Impact of anionic ordering on the iron site distribution and valence states in oxyfluoride Sr2FeO3+xF1−x (x = 0.08, 0.2) with a layered perovskite network

Jacinthe Gamon, Jean-Marc. Bassat, Antoine Villesuzanne, Mathieu Duttine, François Weill, Joke Hadermann, Maria Batuk, Fouad Alassani, Daphne Vandemeulebroucke, Étienne Durand, et al.

Impact of the anionic ordering on the iron site distribution and valence states in oxyfluoride $Sr_2FeO_{3+x}F_{1-x}$ (x = 0.08, 0.2) with layered perovskite network

Jacinthe Gamon,[†,] Jean-Marc Bassat,[†] Antoine Villesuzanne,[†] Mathieu Duttine,[†] Maria Batuk,[‡] Daphne Vandemeulebroucke,[‡] Joke Hadermann,[‡] Fouad Alassani,[†] François Weill,[†] Etienne Durand,[†] Alain Demourgues[†]*

† Univ. Bordeaux, CNRS, Bordeaux INP, ICMCB, UMR 5026, F-33600 Pessac, France

‡ EMAT, University of Antwerp, Groenenborgerlaan 171, B-2020 Antwerp, Belgium

ABSTRACT

Sr_2FeO_3F, an oxyfluoride compound with n=1 Ruddlesden-Popper structure was identified as a potential interesting mixed ionic and electronic conductor (MIEC). The phase can be synthesized under a range of different pO_2 atmosphere, leading to various degree of fluorine for oxygen substitution and Fe^{4+} content. A structural investigation and thorough comparison of both argon and air synthesized compounds was performed by combining high resolution X-ray and electron diffraction, high resolution scanning transmission electron microscopy, Mössbauer spectroscopy and DFT calculations. While the argon synthesized phase shows a well-behaved O/F ordered structure, this study revealed that oxidation leads to averaged large scale anionic disorder on the apical site. In the more oxidized $Sr_2FeO_{3.2}F_{0.8}$ oxyfluoride, containing 20 % of Fe^{4+}, two different Fe positions can be identified with a 32 % / 68 % occupancy ($P4/nmm$ space group). This originates from the presence of antiphase boundaries between ordered domains within the grains. Relations between site distortion and valence states as well as stability of apical anionic sites (O *vs.* F) are discussed. This study paves the way for further studies on both ionic and electronic transport properties of $Sr_2FeO_{3.2}F_{0.8}$ and its use in MIEC based devices, such as solid oxide fuel cells.

MAIN TEXT

1. Introduction

The study of mixed anion compounds emerges as a powerful strategy to modulate material properties and create new functionalities. The arrangement of the anions, having a different charge, electronegativity, size or polarizability in a same structural network governs the geometry of the cation polyhedra (homoleptic or heteroleptic)[1] and their valence states which then influence the

electronic structure of the materials.[2] As such, insertion of fluoride anions into oxide materials appears as an interesting way to modulate the cation oxidation state,[3] and to increase the covalency of the *M*-O bond thanks to the inductive effect procured by the highly electronegative F^- anion. When applied to perovskite related oxides, which are known for their O^{2-} conductivity and their use in solid oxide cells, this substitution could be exploited to modulate electronic and oxygen conductivities as well as surface exchange properties,[4] and in turn decrease operating temperature of devices.

Among oxyfluoride materials, Sr_2FeO_3F type materials stand as interesting compounds for such application, having a good stability in dry air up to 1000°C and sharing a similar structure as well-known Mixed Ionic Electronic Conductors (MIECs) of the nickelate family (Ln_2NiO_4, *Ln* = La, Nd, Pr).[5,6] The crystal structure of $Sr_2Fe^{3+}O_3F$ was first resolved in 1999 by Case et al. by a neutron powder diffraction study, showing that the oxyfluoride crystallizes in an ordered Ruddlesden-Popper *n*=1 Ba_2InO_3F structure type (*P*4/*nmm* space group).[7] The structure can be described as alternating layers of perovskite $SrFe(O,F)_3$ and rocksalt Sr(O,F) slabs, with F and O ordering among the apical positions of the Fe octahedra, forming alternating SrF and SrO rocksalt layers. More generally, all compounds of the Sr_2FeO_3X (*X* = F, Cl, Br) and oxy-halide family adopt the ordered *P*4/*nmm* structure[8]. In contrast, Sr_2MnO_3F,[9] Sr_2CoO_3F[10] and Sr_2NiO_3F,[11] can only be synthesized at high pressure and present the *I*4/*mmm* structure with complete randomization of O and F among the apical site. Tsujimoto et al. showed that some small degree of anionic disorder could be obtained in Sr_2FeO_3F under particularly high pressure conditions while maintaining stoichiometry and homovalent iron states.[12]

Additionally, Menil et al. studied, some years before, the influence of the synthesis atmosphere on the composition and oxidation state of the material.[13] Although the pure stoichiometric $Sr_2Fe^{3+}O_3F$

compound with 100% trivalent iron can be prepared when synthesized under perfectly inert atmosphere, varying quantities of tetravalent iron were found in compounds made under flowing argon or air. Moreover, they found that only the compound made under argon atmospheres presented the extra lines characteristic of the *P*4/*nmm* space group in the diffraction pattern. Conversely, the compound prepared under air showed the *I*4/*mmm* space group, consistent with the 1963 report from Galasso et al.[14] who first synthesized the phase. From these preliminary studies, it can be seen that, in addition to the iron $Fe^{3+/4+}$ compositional change, the synthesis atmosphere has a large impact on the structure of the material. In particular, it can be intuited that oxidation leads to the creation of large scale O/F disorder, responsible for the space group change. Detailed structural investigations concerning the impact of oxidation on the structure are still lacking.

With this in mind, we have performed a structural investigation of the oxyfluoride compound Sr_2FeO_3F and its oxidized counterpart for an in-depth characterization of its peculiar anion defect chemistry, Fe-*X* bonding features and electronic structure.

2. Experimental Section

2.1. Synthesis

Stoichiometric amounts of strontium carbonate ($SrCO_3$, Prolabo 99 %), iron oxide (Fe_2O_3, LTS Chemical Inc. 99.9 %) and strontium fluoride (SrF_2, Merck) were weighted in order to yield a total mass of powder of 5 g. Powders were combined and mixed thoroughly in an agate mortar for 15 min and transferred to an alumina crucible before heating the powder to 1000 °C at a ramp rate of 5 °C·min^{-1}, held at 1000 °C for 12 hours, and then cooled to room temperature at a ramp rate of 5 °C·min^{-1}. The resulting decarbonated mixture was further ground for 15 min, then pelletized in

a 20 mm diameter cylindrical steel die at a pressure of 100 MPa using an uniaxial press, before firing at 1050°C for 24 hours with the same heating and cooling rates. This procedure was repeated twice to complete the reaction. Firing was performed either under ambient air (air-SFF sample) or under flowing argon (Ar-SFF sample) in order to tune the Fe^{4+} content. The Ar-SFF sample was handled in an argon filled glovebox in between each firing step to prevent oxidation.

2.2. Elementary analysis

Inductively coupled plasma optical emission spectroscopy (ICP-OES)

Powder samples were mineralized by dissolution in aqueous HNO_3 (> 68%, 5 mL) HCl (34-37 %, 3 mL) under pressure with microwave heating using an Anton-Paar Multiwave Pro apparatus. ICP-OES measurements were performed using a 5110 Agilent VDV apparatus.

Fluorine titration with specific electrode

Powder samples were mineralized by dissolution of ~80 mg of the sample in 2.5 mL of aqueous HCl (37 w%) at room temperature followed by the addition of 5 mL of the TISAB III complexing agent solution (Sigma Aldrich) and 17.5 mL of deionized water. The solution was then diluted by 10 using a 10 w% sodium acetate buffer aqueous solution in order to increase the pH above 5. For the preparation of the standard solutions, a background solution containing the Fe and Sr cations was first prepared. To that aim, 211 mg of iron nitrate nonahydrate (Sigma Aldrich, > 98 %) and 154 mg of strontium carbonate ($SrCO_3$, Prolabo 99 %) were dissolved in 5 mL of aqueous HCl (37 w%) followed by the addition of 5 mL of the TISAB III complexing agent and 35 mL of deionized water. 5×10^{-2} M, 10^{-2} M, 5×10^{-3} M and 10^{-3} M NaF solutions were prepared by diluting a commercial 10^{-1} M NaF analytical standard solution (Sigma Aldrich) with the background solution. Then, each standard was diluted by 10 using the 10 w% sodium acetate buffer aqueous

solution. Fluorine content was then determined using the perfectION™ Combination Fluoride Electrode (Mettler Toledo).

2.3. X-ray Diffraction

Routine analysis of phase purity and lattice parameters were performed on a PANalytical X'Pert Pro diffractometer with a Cu source (Kα1, λ = 1.54060 Å) in reflection mode. Rietveld quality scans were acquired in powder transmission Debye Scherrer geometry (capillary) with sample rotation to avoid preferential orientation. A Bruker D8 Discover diffractometer with Mo source was used for the Ar-SFF sample, with the sample diluted with borosilicate glass powder (50 w%) and loaded in a Ø = 0.5 mm borosilicate glass capillaries. Synchrotron X-ray diffraction (SXRD) was performed for air-SFF at the 11-BM beamline at Argonne National Laboratory (Argonne, U.S.A), with an incident wavelength of 0.4581020 Å using a multi-analyzer detection assembly (Si (111) crystal analyzers with $LaCl_3$ scintillation detectors), and samples loaded in Ø = 0.8 mm Kapton capillary tubes.

The structural models were refined by the Rietveld method as implemented in the FullProf suite.[15] Peak shapes were modelled using the Thompson-Cox-Hastings function. For the sake of realism, all uncertainties were increased by Berar's factor[16] (2.4 and 4.7 for Ar-SFF and air-SFF, respectively, according to FullProf).

Bond Valence Sump (BVS) Calculation were performed thanks to the program BondStr available within the FullProf Suite. This method is based on the hard sphere model of ions and related the bond valence to the bond length using an empirical bond valence parameter as tabulated by Brese and O'Keefe.[17]

2.4. Electron Diffraction and High-Resolution Transmission Electron Microscopy

Electron diffraction patterns were obtained using a JEM 2100 (JEOL) equipped with an Orius 200D camera (Gatan) and operated at 200kV. High angle annular dark field (HAADF) and annular bright field (ABF) scanning transmission electron microscopy (STEM) images were acquired using a probe aberration corrected FEI Titan 80-300 "cubed" microscope operated at 300 kV.

Prior to their characterizations, the sample was prepared by grinding the material in ethanol, dispersing the solution using the ultrasonic bath and drop casting few drops of the obtained solution onto a carbon-coated Cu TEM grid.

2.5. ^{57}Fe Mössbauer Spectroscopy

Mössbauer experiments were performed in transmission geometry with a constant acceleration (Halder-type) spectrometer equipped with a ^{57}Co(Rh) radioactive source (nominal activity: 1.85 GBq) at room temperature. ^{57}Fe Mössbauer spectra of thin absorbers containing about 5 mg·cm^{-2} of iron were recorded at room temperature (293 K) and the hyperfine parameters (δ isomer shift, Δ quadrupole splitting, Γ Lorentzian linewidth) and relative area of each component were refined using the WinNormos software (Wissenschaftliche Elektronik GmbH). Isomer shift values are relative to α-Fe^0 at room temperature.

2.6. Computational Procedure

Our calculations are based on density functional theory (DFT) and were performed with the Vienna Ab initio Software Package (VASP).[18–20] A *Γ*-centered regular mesh was employed to sample the Brillouin zone with a density of 27 Å^{-1} (for hybrid functional calculations) and 54 Å^{-1} (for GGA+*U* calculations) and a 400 eV cut-off energy was used.

A first calculation using a Hartree-Fock/DFT HSE06 hybrid functional [21,22] was performed with the ordered Sr_2FeO_3F structural model (Figure S10a, *P*4/*nmm*) in order to get the most accurate electronic density. The composition of the unit cell was $Sr_4Fe_2O_6F_2$, and lattice parameters were

fixed to the experimental values obtained from the Rietveld refinement of Ar-SFF (a = 3.8578 Å, c = 13.129 Å). Electron energies were converged to 10^{-3} eV/cell using the tetrahedron method with Blöchl corrections and spin-polarized type calculations (collinear). The quasi-Newton (variable metric) algorithm was used for atomic relaxation (z position only, according to space group symmetry) and total energies were converged to 10^{-2} eV/Å for ionic relaxation. Antiferromagnetic interactions were not considered in the calculation.

As the hybrid functional method is computationally expensive, the GGA+U method (according to the Dudarev et al. scheme)[23] was then conducted using the same convergence criteria and smearing methods as the hybrid calculations throughout. The calculations were first performed using the Sr_2FeO_3F ordered structure and the ionic positions were fixed to those obtained with the previous method. The empirical U parameter for the Fe 3d orbitals was then optimized as to match the electronic bandgap obtained with the hybrid approach.

Figure S11 presents the density of states (DOS) plot of Sr_2FeO_3F obtained with the hybrid and GGA+U methods, showing the good agreement between both results and thereby validating the use of the GGA+U approach for the study of this system. The GGA+U method was then employed to get the electronic properties of two disordered structures with super cells 2a×2b×c (Figure S10b, c). For these, the ionic positions (z position only) were relaxed according to the quasi-Newton (variable metric) algorithm.

The hole effective masses were calculated thanks to the Effmass python package.[24] The effective masses are calculated using the derivatives of a fitted polynomial function using least square method on a band maximum segment of 0.5 eV energy range.

2.7. 4-probe resistivity measurements

Pellets (10 mm diameter) were obtained by uniaxial pressing of the powders (~100 MPa) followed by sintering at 1050°C for 12h under air or Argon atmosphere. Relative densities of ~85 % were obtained for both air-SFF and Ar-SFF. Electrical conductivity was measured with the 4 probe technique in the temperature range 300 °C -600 °C under air.

3. Results

3.1. Synthesis and Composition

Sr_2FeO_3F was synthesized by a classical high temperature solid state route under different synthesis atmosphere, leading to varying oxidation states of the cations, as was studied by Menil et al.[13] Here, we focused our attention on two materials synthesized under argon with $pO_2 \sim 10^{-5}$ atm (Ar-SFF) and under air (air-SFF), and studied the influence of the annealing atmosphere on the composition and structure of the material. The composition of the materials was determined by complementary techniques: (i) ICP/OES results in Sr/Fe ratio of 1.96(6) and 2.02(5), for Ar-SFF and air-SFF, respectively, close to the expected ratio of 2 ; (ii) fluorine ionic specific electrode gives F/Fe ratio of 0.93(6) and 0.84(3) for Ar-SFF and air-SFF, respectively. The oxygen content is approximated by determining the Fe oxidation state through Mössbauer spectroscopy.

3.2. Mössbauer Spectroscopy

^{57}Fe Mössbauer spectroscopy was performed at room temperature to determine the oxidation state and the different environments of iron in the two compounds. Both spectra can be described as the sum of several components (quadrupole doublets) in order to account for the asymmetry of the observed signal and the additional shoulder in between the main doublet, particularly visible for air-SFF. The refined hyperfine parameters of the various quadrupole doublets are reported in Table 1.

For Ar-SFF, the two main components with isomer shift values δ = 0.28(1) mm/s, for type I Fe^{3+}, and 0.36(2) mm/s, for type II Fe^{3+}, can be attributed to high-spin Fe^{3+} in pseudo-octahedral and octahedral environments, respectively. Furthermore, the difference in quadrupole splitting values (0.87 mm/s for type-I Fe^{3+} and 0.25 mm/s for type-II Fe^{3+}) suggests different local environments for Fe^{3+} ions. The quadrupole splitting parameter strongly depends on the electric field gradient (EFG) at the iron nucleus which is influenced in a complex manner by the ligands (O, F), some heterogeneity in Fe-O/F bond length (site distortion) and the nature and distribution of first cationic neighbors. The local environment of type-I Fe^{3+} ions – which appears to be less regular or more perturbed than the type-II Fe^{3+} one – can be attributed to the well-ordered square pyramidal FeO_5F environment, following the results obtained by Menil et al. in the perfectly stoichiometric Sr_2FeO_3F phase.[13] The reconstruction of the experimental spectrum was significantly improved considering an additional component with refined hyperfine parameters (δ = -0.05 mm/s and Δ = 0.18 mm/s) consistent with six-fold coordinated Fe^{4+} ions.

A similar analysis was performed for the air-SFF Mössbauer spectrum, which can also be reconstructed with two Fe^{3+} (δ = 0.26 and 0.35 mm/s) and one Fe^{4+} (δ = -0.02 mm/s) components. Attribution of type II Fe site environment will be discussed in section 4 in light of the results obtained with the other complementary technics: HR-STEM, Rietveld refinement and DFT calculations. Fe^{4+} contents of 8(2) % and 20(3) % were found, for Ar-SFF and air-SFF, respectively. These results are also in good agreement with the report from Menil et al., which shows that the Fe^{4+} content matches that of F loss during synthesis. ~~Therefore, our compounds can be described by the general approximated formulae $Sr_2FeO_{3.07}F_{0.93}$ for Ar-SFF and $Sr_2FeO_{3.2}F_{0.8}$ for air-SFF, respectively.~~

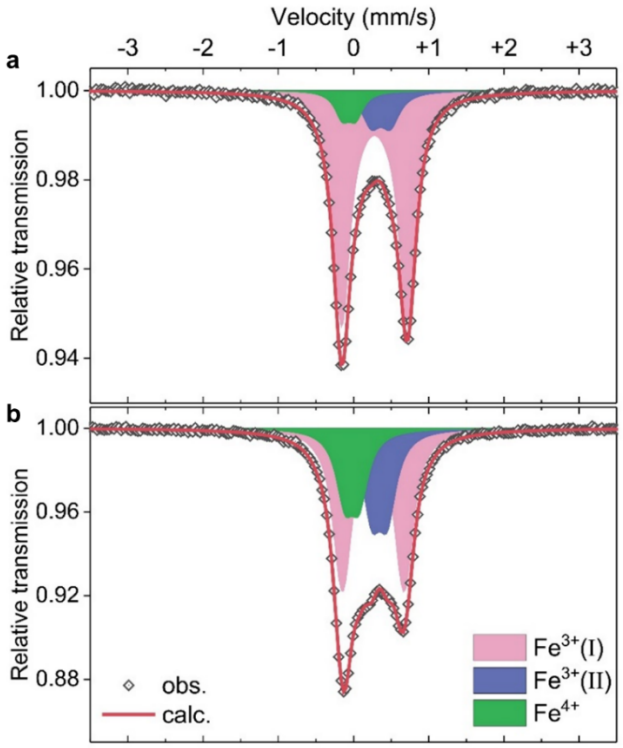

Figure 1. ^{57}Fe Mössbauer spectra of Ar-SFF (a) and air-SFF (b) at 293 K, with the experimental data as black outlined diamonds (obs.), the calculated spectra as a red lines (calc.) and the different components (quadrupole doublets) as filled colored areas.

Table 1. ^{57}Fe Mössbauer hyperfine parameters (293 K)

		δ (mm/s)	**Δ (mm/s)**	**Γ (mm/s)**	**Area (%)**
Ar-SFF	Fe^{4+}	-0.05(2)	0.18(2)	0.25(2)	8(2)
	Fe^{3+}(I)	0.28(1)	0.87(3)	0.28(1)	79(3)
	Fe^{3+}(II)	0.36(2)	0.25(2)	0.31(3)	13(3)
air-SFF	Fe^{4+}	-0.02(2)	0.20(2)	0.29(3)	20(3)
	Fe^{3+}(I)	0.26(1)	0.82(1)	0.30(1)	55(3)
	Fe^{3+}(II)	0.35(1)	0.21(1)	0.28(2)	25(3)

3.3. Diffraction

The diffraction patterns of Ar-SFF and air-SFF can be indexed to the *P*4/*nmm* and *I*4/*mmm* space group, respectively (Le Bail fit shown in Figure S1a and b), consistent with previous reports, as stated in the introduction. For air-SFF, the *hkl* extinctions due to the lattice mode *I* can be observed clearly on Figure 2a and Figure S2. Lattice parameters of air-SFF (a = 3.84759(1) Å; c = 13.0546(1) Å) are smaller than that of Ar-SFF (a = 3.8578(3) Å, c = 13.129(1) Å), leading to a volume shrinkage of 1.010(1) %, consistent with the higher amount of Fe^{4+}, which atomic radius is smaller than that of Fe^{3+} ($r_i(Fe^{4+}_{VI})$ = 0.585 Å ; $r_i(Fe^{3+}_{VI,\ HS})$ = 0.645 Å).[25] Small amounts of impurities of SrF_2 (~1.5 w% = 3.5 mol%) and $Sr_3Fe_2O_7$ (~ 1 w% = 0.6 mol%) were found in the Ar-SFF sample and these were added to the refinement. By neglecting the latter, this would indicate that the Ar-SFF compound is slightly Sr deficient showing an actual composition $Sr_{2-y}FeO_{3.07}F_{0.93-2y}$, with $y \sim 0.03$. In air-SFF, small amounts of the cubic $SrFeO_{3-\delta}$ phase (~2 w% = 3.6 mol%) were found which could indicate a small amount (~4 %) of Fe deficiency in air-SFF. Our Rietveld refinement failed to identify such defects with high enough accuracy, but this should be the object of further study. Moreover, these impurities are susceptible to present tetravalent iron which could contribute to the Fe4+ signal found in the Mossbauer spectra. Considering the amount of impurities determined through Rietveld refinement, these cannot account for more than 1.2 % and 3.6 % of the total Mossbauer signal area for Ar-SFF and air-SFF, respectively. This lies well below the amounts of Fe^{4+} of 8 % and 20 %. Therefore, the main contribution to the Fe^{4+} signal is indeed ascribed to the Sr_2FeO_3F phase, but the error on its actual amount is raised by the presence of these impurities. Therefore, our compounds can be described by the general approximated formulae $Sr_2FeO_{3.08}F_{0.92(2)}$ for Ar-SFF and $Sr_2FeO_{3.2}F_{0.80(4)}$ for air-SFF.

Electron diffraction was performed to check the validity of the space group attribution for both samples (**Figure 2**b, c). Ar-SFF sample could be indexed unambiguously to the *P*4/*nmm* space group (**Figure 2**b). Indeed, spots indexed as 100 or 010 for instance, are clearly observed. On the diffraction patterns obtained for air-SFF (**Figure 2**c), the main spots are consistent with the *I*4/*mmm* space group previously found by XRD, but additional weak blurry spots (yellow arrows on **Figure 2**c) are observed. They are not compatible with the *I*4/*mmm* space group, and a *P* lattice mode must be used to take them into account. In *P*4/*nmm* space group, the F/O ordering is responsible for the lower symmetry of the phase compared to classical K_2NiF_4 *n*=1 RP compounds, with *I*4/*mmm* space group. The additional spots in the ED pattern along with the apparent *hkl* extinction corresponding to the *P*4/*nmm* space group in the XRD data can therefore find its origin in complex arrangement of F/O anions.

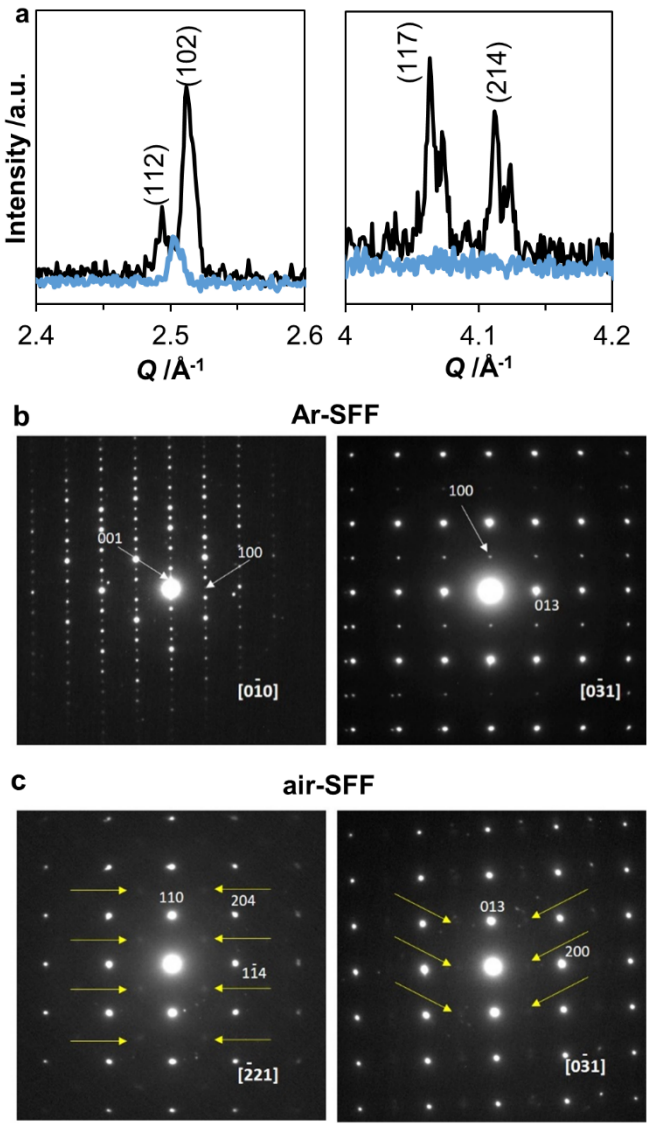

Figure 2. (a) Laboratory X-ray diffraction pattern of Ar-SFF (black line) and air-SFF (blue line) on two different *Q* range. (b, c) Electron diffraction patterns of Ar-SFF (b) indexed with *P*4/*nmm* space group and air-SFF (c) with indexation of the spots in the *I*4/*mmm* space group. The yellow arrows emphases the presence of weak spot contradicting the *I*4/*mmm* space group.

Long range structural models were obtained by Rietveld refinements. The ordered structure described previously (*cf.* introduction, **Figure 3**b) was confirmed for Ar-SFF. Result of the fits are presented in Table S1, S2 and S3 along with the final refinement in **Figure 3**a. Cation site

occupancy factors (*sof*) were refined independently and converged to 1.04(1), 0.98(1) and 0.98(1) for Sr1, Sr2 and Fe, respectively. These were therefore fixed to 1 for the final refinement. Iron sits in a square pyramidal environment with one long and one short Fe-X (X = O, F) apical distance of 2.759(15) Å and 1.926(12) Å, respectively. Attribution of O or F to either of the anionic positions can be classically done thanks to bond valence sum (BVS) calculations (Table S4), with the most probable configuration satisfying a long Fe-F distance and a short Fe-O distance (**Figure 3**c). Fe site splitting could not be identified as the fit using a model with two Fe sites lead to X^2 = 1.93 and R_{bragg} = 2.65 (compared to 1.94 and 2.64 using the model with one Fe site). Synchrotron and neutron diffraction data would be needed to seek for small amounts of Fe site splitting with this method.

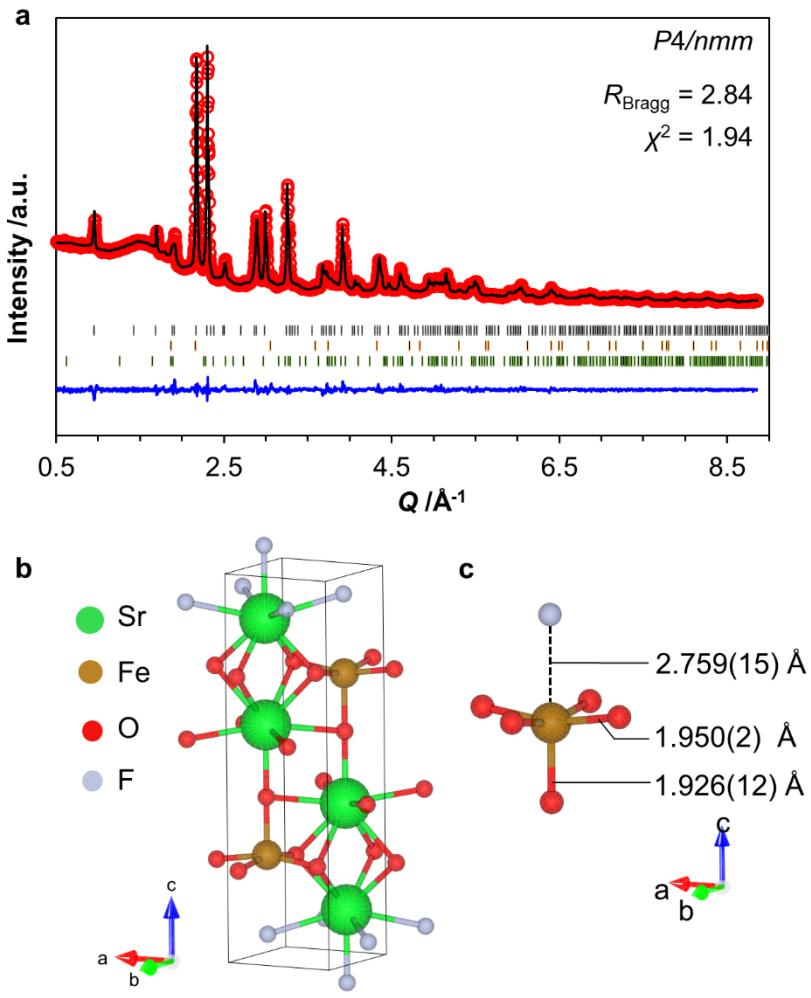

Figure 3. (a) Final Rietveld refinement against the laboratory X-ray diffraction data of Ar-SFF (Bruker, Mo source), with I_{obs} (red dots), I_{calc} (black line), I_{obs}-I_{calc} (blue line), and Bragg reflections (grey tick marks for SFF, orange tick marks for SrF_2 (~1.5 w%) and green tick marks for $Sr_3Fe_2O_7$ ~1 w%)). The broad background contribution comes from the borosilicate glass with which the sample is diluted. (b) Crystal structure of Ar-SFF, (c) Fe square pyramidal environment.

High resolution powder synchrotron X-ray diffraction (SXRD) was obtained on air-SFF. A Rietveld refinement using the typical *P*4/*nmm* space group gave rise to a structural model where iron sits in an axially elongated octahedral site, with two close Fe-*X* (*X* = O, F) apical distances of

2.147(3) and 2.332(3) Å, very close to what is obtained using the *I*4/*mmm* space group (Figure S3, Table S5, S6, S7). Here, the location of F and O atoms cannot be clearly identified through BVS calculations (Table S8), suggesting the possibility of F/O disorder among the apical sites. This differs from the model obtained for Ar-SFF where iron resides in a pseudo square pyramidal environment.

In order to gain more insight into deviation for the ideal structure, the Maximum Entropy Method (MEM) was used to reconstruct the electron density map from the set of observed structure factors to get a less noisy, strictly positive density map compared to that obtained from classical Fourier synthesis. The thus obtained electron density map showed some unexplained density above and below the Fe site along the *c* axis (c). This could either be modelled using anisotropic displacement parameters or by the splitting of the Fe atom into two positions of different *z* coordinates along the *c* axis. The latter option was preferred to better reflect the local environment of the atoms. The model was modified accordingly and this led to a considerable improvement of the fit with R_{Bragg} and χ^2 decreasing from 10.8 and 5.00 to 4.90 and 3.10, respectively. Moreover, residual electron density was found above and below the apical anion site (indicated by yellow arrows on **Figure 4**c), which could further suggest that anion sites are split. However, for the sake of simplicity, and as it did not lead to a major improvement of the fit, the apical anion site was maintained as is.

The *sof* of all atoms were refined independently and converged to 1.005, 1.006, 0.648, 0.345, 1.010, 1,014, 1.019, for Sr1, Sr2, Fe1 and Fe2, O1, $X_{\mathrm{ap}}1$ and $X_{\mathrm{ap}}2$ respectively. Therefore, all *sof* were fixed as full occupancy on each site for the final refinement. The final Rietveld refinement is shown on **Figure 4**a. The result of the fit and the final structural model are presented in Table S9, S10 and S11 and **Figure 4**. Figure S4 shows that the additional peaks due to *P* lattice mode can be well reproduced by the model. The site occupancy factor of both Fe sites, for which the sum was

constrained to full occupancy, lead to 32(1) % / 68(1) % distribution. The location of O and F anions on each of the apical position around the Fe atoms was determined through BVS calculations, leading to the Fe environments shown on **Figure 4**d. It has to be noted that as ~0.2 oxygen atoms exchanged with F atoms during oxidation in air, ~20 % of the Fe atoms should be in a FeO_6 environment. Therefore, locally, these Fe atoms are likely to adopt an elongated octahedral configuration. Additionally, the Sr-Sr projected distance within the rocksalt layer changes significantly compared to the well-ordered phase (Figure S5). Whereas in Ar-SFF, it varies strongly from 3.13 Å (within an SrF rocksalt layer) to 2.88(1) Å (within an SrO layer), in air-SFF, the difference is small, with Sr-Sr projected distances between two consecutive layers of 2.88(1) Å and 2.93(1) Å.

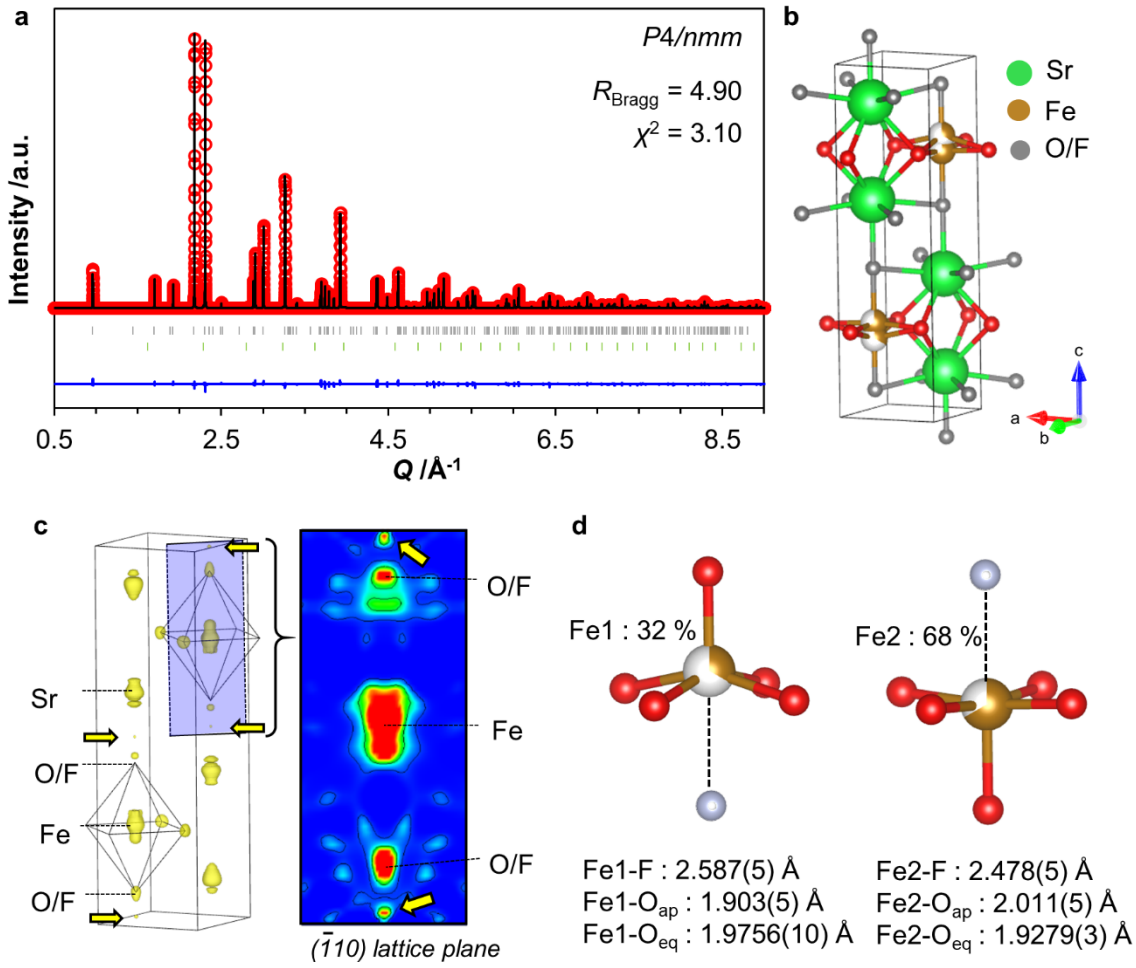

Figure 4. (a) Final Rietveld refinement against the synchrotron X-ray diffraction data of air-SFF (Argonne National Laboratory, 11bm beamline), with I_{obs} (red dots), I_{calc} (black line), I_{obs}-I_{calc} (blue line), and Bragg reflections (grey tick marks for SFF and green tick marks for $SrFeO_{3-\delta}$ (2 w%)). (b) Crystal Structure of air-SFF. (c) Electron density map of air-SFF extracted through the Maximum Entropy Method (using the simple *P*4/*nmm* space group structural model, with one Fe site, obtained from Rietveld refinement (Figure S3c)). Yellow arrows indicate residual electron density close to the apical anion position. (d) Fe square pyramidal environments resulting from the splitting of the site.

3.4. High Resolution Transmission Electron Microscopy

HAADF-STEM images were acquired from different crystals of Ar-SFF and air-SFF and at different orientations (**Figure 5**a, b). For both samples, the images show well-ordered n = 1 structure (no blocks with other "n" or intergrowths were present). We observe a difference in darkness in the layers between two perovskite blocks. For Ar-SFF, the contrast difference alternates every layer (highlighted by the black and grey arrows on **Figure 5**a), however, for air-SFF, the contrast at first sight appears to be random, but alternates within small areas (for example **Figure 5**d). The alternation is clearer from the alternation in the depth of the valleys on the profile plot in **Figure 5**e, as these correspond to the dark layers in the images, the lowest ones being F-F interfaces, the less deep ones O-O interfaces.

The intensity maxima correspond to the Sr positions and the FeO_2 layer shows up as a shoulder to one of the two Sr peaks, indicating it is closer to one peak than the other (white arrows show the shift on **Figure 5**d). The position of the shoulder alternates towards the upper and lower rocksalt layer along the *c* axis, indicating the alternation of the O-O (closer to Fe, layers numbered 2, 4 and 6) and F-F (further away from Fe, numbered 1, 3 and 5) interfaces. Moreover, the Sr-Sr projected distance, plotted in **Figure 5**f, varies systematically from 3.2(1) Å (layers numbered 1, 3 and 5, visually darker interfaces) to 2.9(1) Å (layers numbered 2, 4 and 6, less dark interfaces). The F-F interface is visually darker due to the fact that the bright Sr atoms are further away than for the O-O interface. This matches the distances obtained from the crystallographic ordered model (Figure S5), for which the long distance corresponds to an F-F interface and the short distance to a O-O interface. Therefore, in this area, the position of the Fe peak, the Sr-Sr projected distances and the alternation of the darkness at the interfaces indicate locally ordered domains, with alternation of F-F and O-O interfaces along the *c* axis. Further visualization of these areas can be observed on Figure S6 in [100] and [110] projection and profiles in Figure S7 and S8.

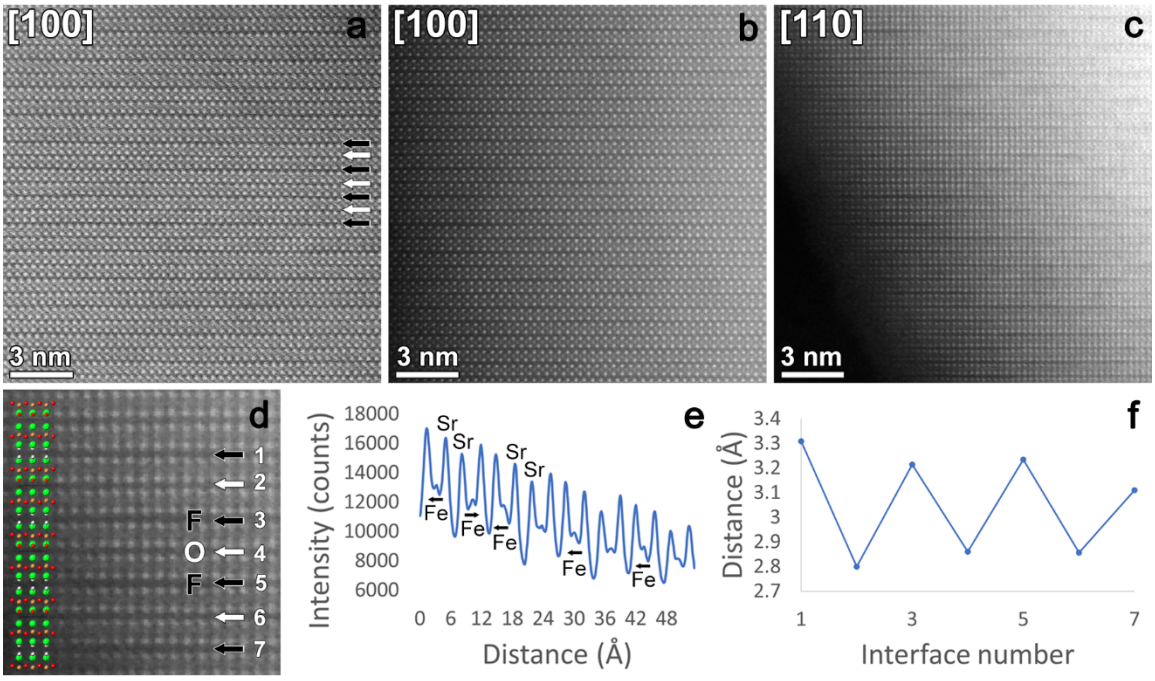

Figure 5. HAADF-STEM images of (a) Ar-SFF and (b,c) air-SFF. (d) Zoom on air-SFF HAADF-STEM image from an area where an alternation of interlayer darkness is observed (layers numbered 1, 3, 5 and 7 appear darker than layers numbered 2, 4 and 6) with associated structural model in inset. (e) Integrated intensity profile measured along the *c* axis of (d). (f) Sr-Sr distance at the interface measured from the intensity profile.

Although we see the expected layer contrast alternation over small domains, for air-SFF, we also observe antiphase boundaries (APB), where the unit cell is shifted over half of the *c* axis (**Figure 6**a) and thus the O-O interface switches to an F-F interface (and vice versa) at the same position along *c*. The intensity profiles were also measured over a large area of 20 nm corresponding to around 15 unit cells (Figure S7 and S8), and the O-O versus F-F alternation is clear on the Ar-SFF images, but less clear and shorter ranged on the air-SFF images. The unclear alternation of Sr-Sr distances and Fe shifts in air-SFF is probably due to the APB giving overlaps of O-O and F-F interfaces in projection. The position of the Fe atoms towards the O and away from the F rocksalt

layer is also directly seen on the ABF-STEM images on **Figure 6**b, with the shift highlighted by the white arrows. Again, the observed shift is only ordered over small areas. Further visualisation of the ordered Ar-SFF versus APB dense air-SFF is given by the inverse Fourier transforms (iFFT) (**Figure 6**e,f) taken of only the 001/00$\bar{1}$ reflections of the FFT of the images (Figure S9). Such iFFT reveals the periodicity along the *c*-axis. For Ar-SFF we observe straight lines with a periodicity equal to the *c*-parameter of the unit cell, while for air-SFF the lines are regularly interrupted and shifted over half a unit cell, corresponding to APBs.

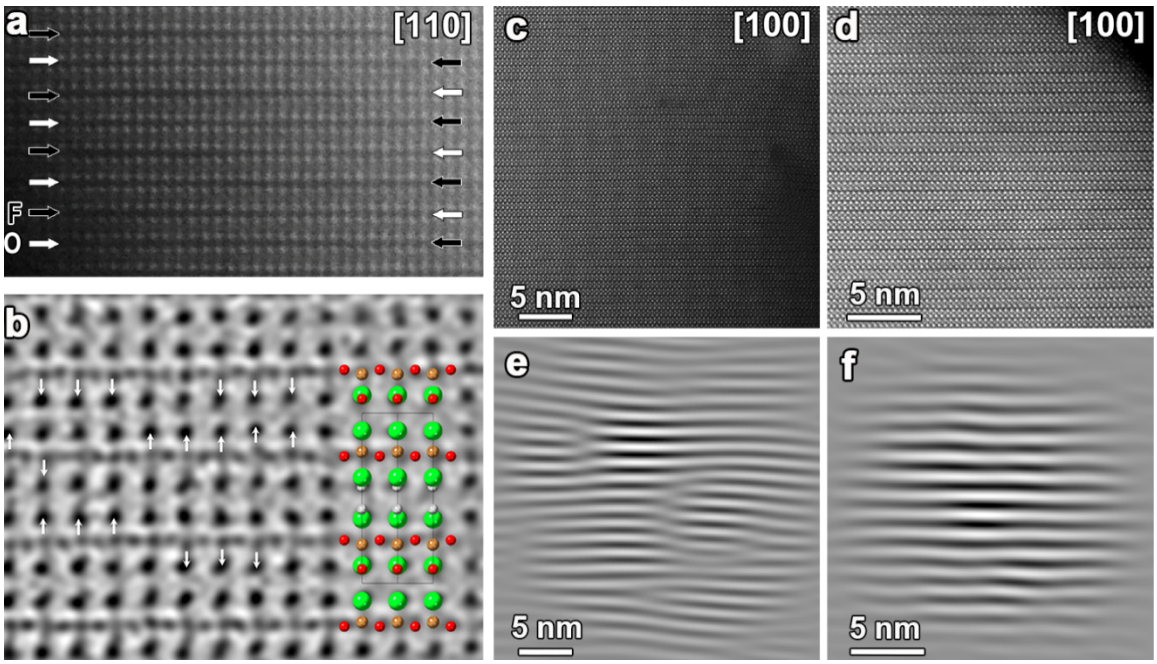

Figure 6. (a) APB defect observed in the [110] HAADF-STEM image of air-SFF. (b) ABF-STEM image of air-SFF with associated structural model showing the displacement of the Fe atom toward one rocksalt layer (indicated by white arrows). The tails of the arrows end on the corresponding atoms and the arrow heads show the shift direction. [100] HAADF-STEM images of (c) air-SFF and (d) Ar-SFF. Inverse FFT with a mask leaving only the 001 and 00$\bar{1}$ reflections in the FFT of the [100] HAADF-STEM image of (e) air-SFF and (f) Ar-SFF (*cf.* SI, Figure S9).

3.5. DFT Calculations

3.5.1. Ordered Sr_2FeO_3F ($Sr_4Fe_2O_6F_2$)

The electronic structure calculation was performed on the stoichiometric compound Sr_2FeO_3F. The unit cell composition was $Sr_4Fe_2O_6F_2$ and the lattice parameters were fixed to the experimental values obtained for Ar-SFF. Starting from the structural model obtained with Rietveld refinement, the *z* position of all atoms was relaxed and this converged to a structural model with the expected long Fe-F and short Fe-O distances: 2.679 Å and 1.915 Å, respectively, close to the experimental values. The structural model is displayed on Figure S10. Moreover, the Sr-Sr projected distance between two consecutive rocksalt slabs (Figure S12) is in very good agreement with the experimental values (Figure S5). These results confirmed the attribution of F and O positions in the Rietveld structural model based on the BVS calculation.

Figure 7a presents the density of states of Sr_2FeO_3F showing that the compound is a semiconductor with a spin inversion band gap of ~1.5eV between spin up Fe(3*d*)-O(2*p*) orbitals and spin down Fe(3*d*) orbitals. The top of the valence band is further visible on **Figure 7**c, where the contribution from apical and equatorial oxygen was split. A very interesting feature arises from the shape of the valence band maximum (VBM) which is highly dispersed, over more than 1.5 eV. This comes from the strong hybridization of iron 3*d* orbitals and equatorial oxygens 2*p* orbitals. The band structure *E* vs. *k* is plotted on **Figure 7**b and shows that the bandgap is indirect with the top of the valence band located at the *M* point and the bottom of the conduction band at the *Γ* point of the Brillouin zone. The strong dispersion of the top of the valence band is further visualized through the strong curvature of the band at the *M* point. The hole effective masses in the *X*-*M* [100] and *Z*-*A* [110] directions were calculated with the Effmass open-source package[24] and values of -0.65 m_e and -0.72 m_e for [100] and [110] directions, respectively, were obtained (Table 2). Due to the strong band dispersion and hybridization, these values are remarkably low among oxides

compounds for which the VBM is often mostly constituted of non-bonding, localized oxygen 2*p* orbitals.[26-28] This noteworthy characteristic is of strong interest for applications seeking for high electronic hole mobility such as electrode materials.

Table 2. Hole effective mass in [100] direction /m_e calculated with Effmass program[24]

Structure	Ordered $Sr_4Fe_2O_6F_2$	*Disordered* $Sr_{16}Fe_8O_{24}F_8$ *#1*	*Disordered* $Sr_{16}Fe_8O_{24}F_8$ *#2*
Hole effective mass /m_e	-0.65 ([010]) -0.72 ([110])	-0.67 ([100])	-0.64 ([100])

3.5.2. Disordered Sr_2FeO_3F ($Sr_{16}Fe_8O_{24}F_8$)

To assess the effect of anion apical disorder on the electronic structure and atomic position of the compound, DFT calculations were performed using a structural model with the unit cell $2a \times 2b \times c$, multiplied by four compared to the parent ordered compound. Apical oxygen and fluorine atoms were manually randomly swapped over the 16 positions to get two different model disordered structures (#1 and #2, Figure S10), so that three types of Fe octahedra are formed: FeO_5F, FeO_6 and FeO_4F_2. The *a* and *c* parameters were fixed to the experimental values obtained for air-SFF, and atomic positions were relaxed using the DFT+*U* method (with $U = 6$ eV for Fe). Interestingly, the Fe-*X* (*X* = O_{eq}, O_{ap}, F) distances vary compared to the ordered compound, even within the FeO_5F octahedra. The averaged distances for the three Fe environment types are reported in Table S14. For both disordered structures, in the FeO_5F octahedra the Fe-O_{ap} distances increase whereas the Fe-O_{eq} and more particularly the Fe-F distances decrease, compared to the ordered structure. Moreover, in the FeO_6 and FeO_4F_2 octahedra, the Fe-O_{eq} distances decrease compared to the ordered structure and the two Fe-X_{ap} relax to similar values, so that Fe resides in an elongated octahedral environment.

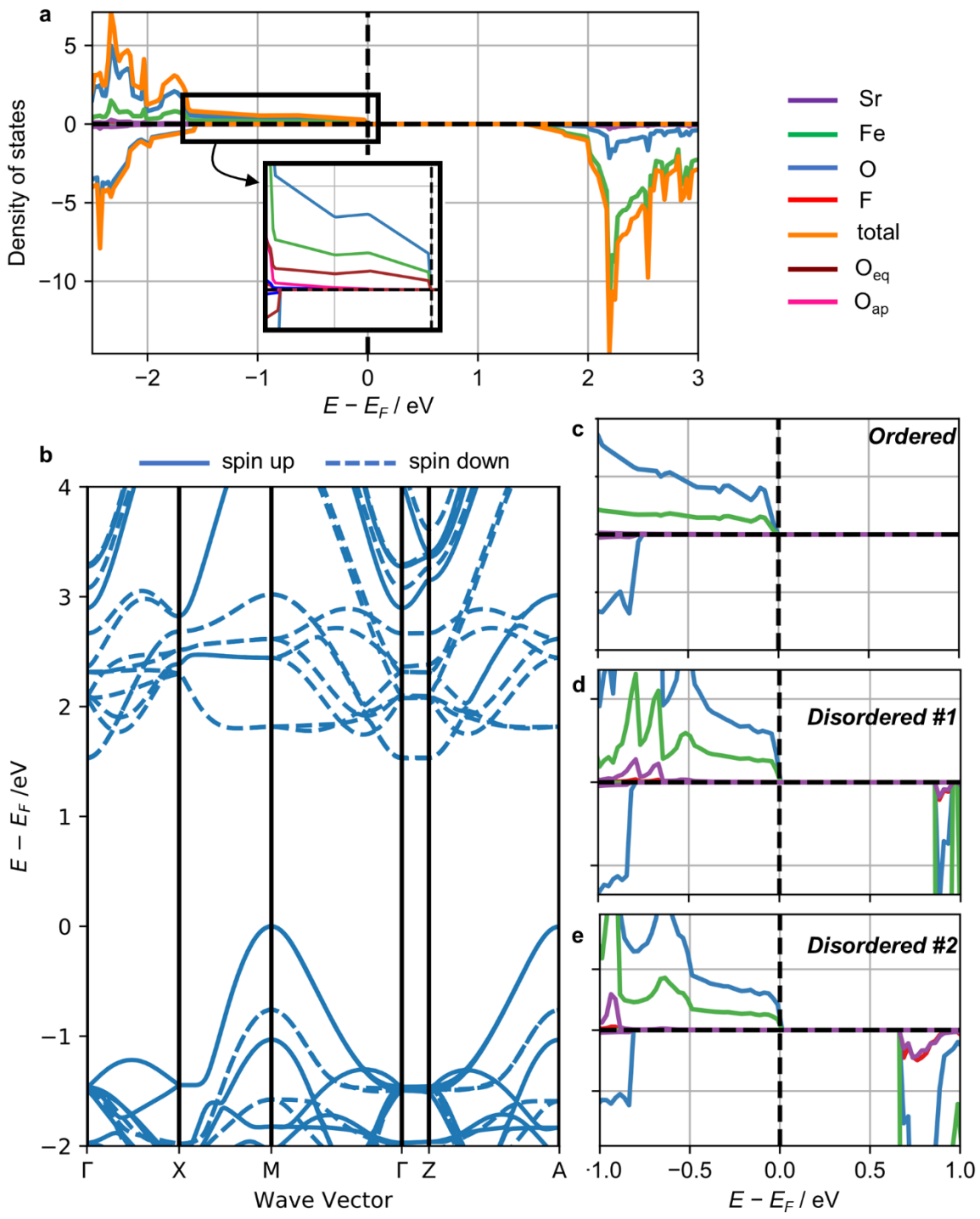

Figure 7. (a) Density of states of ordered Sr_2FeO_3F calculated with the DFT/HSE06 method, (b) electronic band structure calculation for ordered Sr_2FeO_3F calculated with the GGA+ U method (U = 6 eV for Fe 3d orbitals), (c, d, e) Zoom of the top of the valence band in the density of state

of ordered (c) and disordered Sr_2FeO_3F structures (d and e) (Figure S10) calculated with GGA+ *U* method (normalized intensities).

The impact of disorder on the density of states and on the electronic band structure is limited. **Figure 7**c-e show that the band gap decreases, and the strong dispersion at the top of the valence band comprising the hybridization of the Fe-3*d* and O2*p* is maintained. Here, the top of the valence band is located at the *Γ* and *Z* points for both disordered structures (Figure S13), thereby the VBM presents a dispersed and a flat band contribution in the *Γ*-*X* [100] and *Γ*-*Z* [001] directions, respectively. The electronic hole effective mass along the [100] direction remains close to the values calculated for the ordered structure (Table 2).

4. Discussion

The average formulae of Ar-SFF and air-SFF are $Sr_2Fe^{3+}_{0.93}Fe^{4+}_{0.07}O_{3.07}F_{0.93}$ and $Sr_2Fe^{3+}_{0.8}Fe^{4+}_{0.2}O_{3.2}F_{0.8}$, respectively. In both compounds, the total anion content is close to 4, and oxidation of the air-SFF material occurs via an oxygen for fluorine substitution, rather than oxygen insertion within interstitial sites, thereby giving the general formulae $Sr_2Fe^{3+}_{1-x}Fe^{4+}_{x}O_{1+x}F_{1-x}$, with $x = 0.07$ and 0.20, giving rise to x % of Fe atoms surrounded by six oxygen anions. The identification of Fe^{4+} species through Mössbauer spectroscopy indicates that charges are localized rather than delocalized with iron in mixed valence state. Moreover, the localization of these x % Fe^{4+} species is expected to be more energetically favorable within the x % FeO_6 octahedra due to the stronger crystal field effect of O^{2-} vs. more electronegative F^-. The result of the BVS calculation in the DFT disordered structure reinforces this assumption, showing that the FeO_6 octahedra show a significantly higher BVS compared to the other two sites FeO_5F and FeO_4F_2 (Table S14).

Along with the typical signal of Fe^{3+} in square pyramidal environment (type I), the Mössbauer spectra of both compounds showed the signature of an additional more symmetric and higher coordination Fe^{3+} environment (type II). This contribution could be attributed to Fe^{3+} species which have at least one $Fe^{4+}O_6$ as first neighbors. Indeed, these defects will lead to an homogenization of the electric field, compared to the alternating Sr-F and Sr-O layered structure, thereby affecting both isomer shift and quadrupole splitting parameters of nearby iron species. This matches the DFT calculation results obtained with the disordered model, which showed that the FeO_5F environment becomes less anisotropic, thereby affected by the presence of FeO_6 and FeO_4F_2 nearby octahedra.

Our calculation for the amount of type II Fe^{3+} considering homogeneous distribution or 1D linear channel distribution of $Fe^{4+}O_6$ defects using probability laws failed to match the experimental values (cf. SI, part 4.). This highlights that these defects are not evenly distributed within the crystal, but rather form clusters. HR-TEM analysis reveals the presence of antiphase boundary defects, whose amount considerably increases as the oxygen content increases from 3.08 in Ar-SFF to 3.2 in air-SFF. It is therefore expected that $Fe^{4+}O_6$ defects should be localized close to the antiphase boundaries, which explains an inhomogeneous distribution. The two different environments associated to type I and type II Fe^{3+} reflects the presence of well-ordered areas vs. defect-type areas. These two types of environments are also distinguishable with Rietveld refinement in air-SFF. The Fe1 site is highly anisotropic and close to five-fold coordination, thereby matching the type I Fe^{3+} contribution in the Mössbauer spectra, whereas the type II contribution can be assigned to the Fe2 site from Rietveld refinement which is less anisotropic and closer to six-fold coordination. The amount of type I or Fe1 sites gives an indication of the

percentage of perfectly ordered areas: 50 % and 32 %, respectively. The discrepancy between XRD and Mössbauer results highlights the difference in the scales screened by the different technique.

The goal of the present study was to investigate the structure of Sr_2FeO_3F and its oxidized counterpart with the aim to correlate this investigation to electron and oxide ion transport properties. The structural investigation of $Sr_2FeO_{3.2}F_{0.8}$ (air-SFF) reveals that this material possesses some remarkable peculiar features. Firstly, this oxyfluoride can be synthesized in ambient air, and is stable under this atmosphere up to temperatures as high as 1100 °C, on the contrary to many other oxyfluorides of the RP structure that are synthesized via topotactic fluorination at low temperature of the corresponding oxide. Although the effect of humidity on the chemical stability of the compound has not been genuinely studied, it appears that $Sr_2FeO_{3.2}F_{0.8}$ has a particularly low reactivity towards hydrolysis. Compared to other oxyfluoride materials among the RP family, $Sr_2FeO_{3.2}F_{0.8}$ thereby showcases a strong chemical and thermal stability under air. The creation of large scale disorder for O/F apical anion sites along oxidation is another interesting and original aspect of the material which could have a direct impact on properties such as the apical oxygen anion mobility. Moreover, in this compound, 20% of Fe^{4+} was found by Mössbauer spectroscopy. Such high proportion of Fe^{4+} in oxide compounds are scarce and is believed to have a strong impact on the electronic properties of the material. Indeed, the substitution acts as a p-type doping, with the presence of both Fe^{3+} and Fe^{4+} species and a potentially high electronic hole mobility, considering the high band dispersion at the VBM, if charge delocalization can be triggered. The electronic conductivity of both phases was assessed under air (Figure S16). Due to the poor density of the pellets, the values obtained are not intrinsic to the bulk phase but enable a direct comparison between samples. As expected, both compounds present a semiconducting behavior and an enhancement of electronic conductivity by ~4 orders of

magnitude was obtained in $Sr_2FeO_{3.2}F_{0.8}$ compared to $Sr_2FeO_{3.08}F_{0.92}$. This shows that electronic hopping occurs. However, the conductivity remains moderate: ~0.8 $S \cdot cm^{-1}$ at room temperature for $Sr_2FeO_{3.2}F_{0.8}$In the compounds studied, Fe^{4+} is suspected to be localized within the FeO_6 octahedra, rather than within FeO_5F octahedra. Therefore, a high anionic mobility could be a driving force for Fe^{4+} delocalization, a high electronic mobility, and vice versa. The question remains whether sufficient oxide anion mobility could be obtained in such a phase. For high oxygen anion diffusion, there must be anion vacancies and/or thermodynamically accessible interstitial sites. A high concentration of such defects seemed to remain absent in Ar-SFF and air-SFF as attested by the constant anion content of 4. To increase oxygen and electronic mobility, it would be of high interest to tune the cation content (through substitution with copper for instance or by inducing strontium vacancies) as to create anion vacancies, but also to induce anion over stoichiometry, by populating interstitial sites within the rocksalt layer. The investigation of transport properties in $Sr_2FeO_{3.2}F_{0.8}$ and doped counterparts will be the object of future studies.

5. Conclusion

To conclude, we have performed a thorough structural investigation of Sr_2FeO_3F and its oxidized counterpart $Sr_2FeO_{3.2}F_{0.8}$. In the latter, oxide for fluorine substitution occurs at high temperature under air atmosphere and leads to the creation of large-scale apical anion disorder. Through various complementary technics (Mössbauer spectroscopy, Rietveld refinement against XRD data, HR-STEM and DFT calculations), we were able to characterize the extent of anionic disorder on a large scale as well as at the atomic level. Ordered domains were clearly visible through HR-STEM along with the presence of large amounts of antiphase boundaries, induced by the oxygen for fluorine substitution. The analysis of Fe environments shows the presence of two different sites

within the material: one highly anisotropic, five-fold coordination FeO_5F corresponding to the perfectly ordered areas, and one less anisotropic, encompassing Fe^{3+} species with $Fe^{4+}O_6$ and antiphase boundary defects in their close surroundings. In this compound, the electronic hole mobility is expected to be particularly large, with important hybridization of the Fe 2*p* and O_{eq} 2*p* orbitals along with high band dispersion at the top of the valence band. By triggering oxygen anion mobility through the creation of anion vacancies for instance, and inducing in turns electronic charge delocalization, $Sr_2FeO_{3.2}F_{0.8}$ appears as an appealing candidate for mixed electronic and ionic conductivity (MIEC). Along with a high stability in air and at high temperature, the in-depth structural characterization of this material paves the way for the study of analogous oxyfluorides that could find application as air electrode materials in solid oxide cells requiring such MIEC properties.

ASSOCIATED CONTENT

Supporting Information. Rietveld refinement figures using different structural models, Tables containing outcomes of the refinements with structural models, bond distances and bond valence sum calculations, additional HAADF-STEM images, structural models used for DFT calculation, comparison of DOS plot of Sr_2FeO_3F using HF and GGA+*U* method, bond valence sum calculation resulting from DFT structural models, electronic band structure plots for disordered Sr_2FeO_3F. The following files are available free of charge. (SFF-SI.pdf)

AUTHOR INFORMATION

Corresponding Author

* jacinthe.gamon@icmcb.cnrs.fr

Author Contributions

The manuscript was written through contributions of all authors. All authors have given approval to the final version of the manuscript.

ACKNOWLEDGMENT

We thank Eric Lebrault, Matthew Suchomel and Stanislav Pechev from the ICMCB Diffraction Service for performing laboratory X-Ray diffraction scans. The 11-BM beamline staff at Argonne National Laboratory are acknowledge for performing the SXRD data collection. Use of the Advanced Photon Source at Argonne National Laboratory was supported by the U. S. Department of Energy, Office of Science, Office of Basic Energy Sciences, under Contract No. DE-AC02-06CH11357. Computational resources were provided by the Mésocentre de Calcul Intensif Aquitain (MCIA), University of Bordeaux.

REFERENCES

(1) Charles, N.; Saballos, R. J.; Rondinelli, J. M. Structural Diversity from Anion Order in Heteroanionic Materials. *Chem Mater* **2018**, *30* (10), 3528–3537.

(2) Kuriki, R.; Ichibha, T.; Hongo, K.; Lu, D.; Maezono, R.; Kageyama, H.; Ishitani, O.; Oka, K.; Maeda, K. A Stable, Narrow-Gap Oxyfluoride Photocatalyst for Visible-Light Hydrogen Evolution and Carbon Dioxide Reduction. *J Am Chem Soc* **2018**, *140* (21), 6648–6655.

(3) Harada, J. K.; Charles, N.; Poeppelmeier, K. R.; Rondinelli, J. M. Heteroanionic Materials by Design: Progress Toward Targeted Properties. *Adv. Mater.* **2019**, *31* (19), 1805295.

(4) Zhang, Z.; Zhu, Y.; Zhong, Y.; Zhou, W.; Shao, Z. Anion Doping: A New Strategy for Developing High-Performance Perovskite-Type Cathode Materials of Solid Oxide Fuel Cells. *Adv. Energy Mater.* **2017**, *7* (17), 1700242.

(5) Kharton, V. V.; Marques, F. M. B.; Atkinson, A. Transport Properties of Solid Oxide Electrolyte Ceramics: A Brief Review. *Solid State Ion.* **2004**, *174* (1), 135–149.

(6) Boehm, E.; Bassat, J.; Dordor, P.; Mauvy, F.; Grenier, J.; Stevens, P. Oxygen Diffusion and Transport Properties in Non-Stoichiometric $Ln_{2-x}NiO_{4+\delta}$ Oxides. *Solid State Ion.* **2005**, *176* (37–38), 2717–2725.

(7) Case, G. S.; Hector, A. L.; Levason, W.; Needs, R. L.; Thomas, M. F.; Weller, M. T. Syntheses, Powder Neutron Diffraction Structures and Mossbauer Studies of Some Complex Iron Oxyfluorides: $Sr_3Fe_2O_6F_{0.87}$, Sr_2FeO_3F and $Ba_2InFeO_5F_{0.68}$. *J. Mater. Chem.* **1999**, *9* (11), 2821–2827.

(8) Hector, A.; Hutchings, J.; Needs, R.; Thomas, M.; Weller, M. Structural and Mossbauer Study of Sr_2FeO_3X (X = F, Cl, Br) and the Magnetic Structure of Sr_2FeO_3F. *J. Mater. Chem.* **2001**, *11* (2), 527–532.

(9) Su, Y.; Tsujimoto, Y.; Matsushita, Y.; Yuan, Y.; He, J.; Yamaura, K. High-Pressure Synthesis, Crystal Structure, and Magnetic Properties of Sr_2MnO_3F: A New Member of Layered Perovskite Oxyfluorides. *Inorg Chem* **2016**, *55* (5), 2627–2633.

(10) Tsujimoto, Y.; Li, J. J.; Yamaura, K.; Matsushita, Y.; Katsuya, Y.; Tanaka, M.; Shirako, Y.; Akaogi, M.; Takayama-Muromachi, E. New Layered Cobalt Oxyfluoride, Sr_2CoO_3F. *Chem. Commun.* **2011**, *47* (11), 3263–3265.

(11) Tsujimoto, Y.; Yamaura, K.; Uchikoshi, T. Extended Ni(III) Oxyhalide Perovskite Derivatives: Sr_2NiO_3X (X = F, Cl). *Inorg Chem* **2013**, *52* (17), 10211–10216.

(12) Tsujimoto, Y.; Matsushita, Y.; Hayashi, N.; Yamaura, K.; Uchikoshi, T. Anion Order-to-Disorder Transition in Layered Iron Oxyfluoride Sr_2FeO_3F Single Crystals. *Cryst. Growth Des.* **2014**, *14* (9), 4278–4284.

(13) Menil, F.; Kinomura, N.; Fournes, L.; Portier, J.; Hagenmuller, P. Investigation of the K_2NiF_4,-Type Layer Oxide Fluorides $Sr_2FeO_{3+x}F_{1-x}$ ($0 \leqq x \leqq 0.20$). *Phys. Status Solidi A* **1981**, *64* (1), 261–274.

(14) Galasso, F.; Darby, W. Preparation and Properties of Sr_2FeO_3F. *J. Phys. Chem.* **1963**, *67* (7), 1451-1453.

(15) FullProf Suite - Crystallographic Tool for Rietveld, Profile Matching & Integrated Intensity Refinements of X-Ray and/or Neutron Data, http://www.ill.eu/sites/fullprof/.

(16) Bérar, J.-F.; Lelann, P. E.s.d.'s and Estimated Probable Error Obtained in Rietveld Refinements with Local Correlations. *J. Appl. Crystallogr.* **1991**, *24* (1), 1–5.

(17) Brese, N. E.; O'Keeffe, M. Bond-Valence Parameters for Solids. *Acta Cryst B* **1991**, *47* (2), 192–197.

(18) Kresse, G.; Hafner, J. Ab Initio Molecular Dynamics for Liquid Metals. *Phys Rev B* **1993**, *47* (1), 558–561.

(19) Kresse, G.; Furthmüller, J. Efficient Iterative Schemes for Ab Initio Total-Energy Calculations Using a Plane-Wave Basis Set. *Phys Rev B* **1996**, *54* (16), 11169–11186.

(20) Kresse, G.; Furthmüller, J. Efficiency of Ab-Initio Total Energy Calculations for Metals and Semiconductors Using a Plane-Wave Basis Set. *Comput. Mater. Sci.* **1996**, *6* (1), 15–50.

(21) Heyd, J.; Scuseria, G. Efficient Hybrid Density Functional Calculations in Solids:

Assessment of the Heyd-Scuseria-Ernzerhof Screened Coulomb Hybrid Functional. *J. Chem. Phys.* **2004**, *121*, 1187–1192.

(22) Krukau, A. V.; Vydrov, O. A.; Izmaylov, A. F.; Scuseria, G. E. Influence of the Exchange Screening Parameter on the Performance of Screened Hybrid Functionals. *J. Chem. Phys.* **2006**, *125* (22), 224106.

(23) S. L. Dudarev, G. A. Botton, S. Y. Savrasov, C. J. Humphreys, A. P. Sutton. Electron-energy-loss spectra and the structural stability of nickel oxide: An LSDA+U study. *Phys. Rev. B* **1998**, *57* (3), 1505-1509.

(24) Whalley, L. D. Effmass: An Effective Mass Package. *J. Open Source Softw.* **2018**, *3* (28), 797.

(25) Shannon, R. D. Revised Effective Ionic Radii and Systematic Studies of Interatomic Distances in Halides and Chalcogenides. *Acta Cryst A* **1976**, *32* (5), 751–767.

(26) Hautier, G.; Miglio, A.; Ceder, G.; Rignanese, G.-M.; Gonze, X. Identification and Design Principles of Low Hole Effective Mass P-Type Transparent Conducting Oxides. *Nat. Commun.* **2013**, *4* (1), 2292.

(27) Dahliah, D.; Rignanese, G.-M.; Hautier, G. Defect Compensation in the p-Type Transparent Oxide Ba_2BiTaO_6. *J. Mater. Chem. C* **2020**, *8* (27), 9352–9357.

(28) Norton, D. P.; Heo, Y. W.; Ivill, M. P.; Ip, K.; Pearton, S. J.; Chisholm, M. F.; Steiner, T. ZnO: Growth, Doping & Processing. *Mater. Today* **2004**, *7* (6), 34–40.

TABLE OF CONTENT GRAPHIC

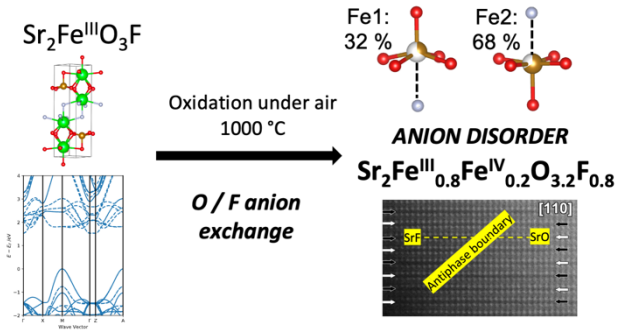

SYNOPSIS

$Sr_2FeO_{3+x}F_{1-x}$ (x = 0.08, 0.2), an n=1 Ruddlesden-Popper phase was synthesized from the oxidation of Sr_2FeO_3F in air at high temperature following a fluorine for oxygen substitution and Fe^{3+} to Fe^{4+} oxidation. A structural investigation of both compounds was performed using complementary and high-resolution technics (Synchrotron X-ray and electron diffraction, Mössbauer spectroscopy, HR-STEM) coupled to DFT calculation. This study reveals that oxidation leads to a high degree of apical anion disorder coupled to antiphase boundaries.